PROTEINS
STRUCTURE ■ FUNCTION ■ BIOINFORMATICS

Antagonist binding and induced conformational dynamics of GPCR A_{2A} adenosine receptor

Xueqin Pang, Mingjun Yang, and Keli Han*

State Key Laboratory of Molecular Reaction Dynamics, Dalian Institute of Chemical Physics, Chinese Academy of Sciences, Dalian, Liaoning 116023, China

The A_{2A} adenosine receptor (A_{2A}AR) is a unique G-protein coupled receptor (GPCR), because besides agonist, its antagonist could also lead to therapeutic relevance. Based on A_{2A}AR-antagonist crystal structure, we have studied the binding mechanism of two distinct antagonists, ZM241385 and KW6002, and dynamic behaviors of A_{2A}AR induced by antagonist binding. Key residues interacting with both antagonists and residues specifically binding to one of them are identified. ZM241385 specifically bound to S67$^{2.65}$, M177$^{5.38}$, and N253$^{6.55}$, while KW6002 binds to F62$^{2.60}$, A81$^{3.29}$, and H264$^{7.29}$. Moreover, interactions with L167$^{5.28}$ are found for both antagonists, which were not reported in agonist binding. The dynamic behaviors of antagonist bound holo-A_{2A}ARs were found to be different from the apo-A_{2A}AR in three typical functional switches, (i) the "ionic lock" was in equilibrium between formation and breakage in apo-A_{2A}AR, but stayed broken in holo-A_{2A}ARs; (ii) the "rotamer toggle switch," T88$^{3.36}$/F242$^{6.44}$/W246$^{6.48}$, adopted different rotameric conformations in apo-A_{2A}AR and holo-A_{2A}ARs; (iii) apo-A_{2A}AR preferred α-helical intracellular loop (IC)2 and flexible IC3, while holo-A_{2A}ARs had a flexible IC2 and α-helical IC3. Our results indicated that antagonist binding induced different conformational rearrangements of these characteristic functional switches in apo-A_{2A}AR and holo-A_{2A}ARs.

Proteins 2013; 81:1399–1410

Key words: A_{2A}AR; molecular dynamics; ZM241385; KW6002; ligand specific binding; ionic lock; rotamer toggle switch; secondary structure.

INTRODUCTION

The G-protein coupled receptors (GPCRs) are transmembrane proteins adopting active and inactive allosteric equilibrium upon extracellular chemical or sensory stimuli.[1] The A_{2A} adenosine receptor (A_{2A}AR) is of special therapeutic interest for the fact that, besides agonist, antagonist can also target at the protein and exert neural functions in the central nervous system.[2] Inhibition of A_{2A}AR relieves nervous system disorders in Parkinson's disease (PD).[3] A_{2A}AR antagonists thus have emerged as a potential non-dopaminergic therapy and attracted great attention in clinical development.[4,5] Furthermore, A_{2A}AR antagonists also showed therapeutic value for treatments of Huntington's disease,[6] epilepsy,[7] and cerebral ischemia,[8] and improve tumor inhibition.[9] However, as for how antagonist binding influences the neurochemical and behavioral interactions of A_{2A}AR, little is known and only two hypothesis contradictory to each other were proposed. The heteromeric dimerization, e.g. direct receptor-receptor interaction of A_{2A}AR/D_2Rs[10] or A_{2A}AR/mGluR5,[11] is proposed as a possible mechanism. On the other hand, studies also suggest that A_{2A}AR exert its nature function partly or entirely independent of D_2Rs, with experiments that blockade[12] or knockout of D_2Rs.[13,14] The molecular mechanism of A_{2A}AR antagonism is far from clear.

The past decades witness exciting achievements in determining molecular structures and dynamics properties of the GPCR family, especially A_{2A}AR. Crystal structures binding with either antagonist[15–17] or agonist[18,19] were published, leading to crucial hints to their functional mechanisms. Meanwhile, computational studies also provided dynamic information that gives further detailed understandings of the receptor functionality. Simulations of A_{2A}AR in both cholesterol-free and cholesterol-bound POPC membrane bilayers suggested that cholesterol could bind with A_{2A}AR at the interface (comprised of TM1, TM2, and TM3) and functioned as a

Additional Supporting Information may be found in the online version of this article.

*Correspondence to: Keli Han, 457 Zhongshan Road, Dalian, Liaoning 116023, China. E-mail: klhan@dicp.ac.cn

Received 6 November 2012; Revised 12 February 2013; Accepted 4 March 2013
Published online 18 March 2013 in Wiley Online Library (wileyonlinelibrary.com).
DOI: 10.1002/prot.24283

cofactor with the agonist in GPCR activation.[20] Conformational dynamics of $A_{2A}AR$ bound with agonist, adenosine or UK432097, revealed that the binding of adenosine was highly dynamical while UK432097 stabilized a much tighter neighborhood of active conformation, and thus explained the 100- to 1000-fold greater efficacy of UK432097 relative to adenosine.[21] In this study, we focus on antagonists instead, illustrating antagonist binding and important $A_{2A}AR$ conformation changes upon antagonism.

The first goal of our study is to identify key $A_{2A}AR$-antagonist interactions in membrane, thereby providing insights for future design in specific antagonist that could enhance $A_{2A}AR$ antagonism. Antagonists of $A_{2A}AR$ are categorized into two classes: the xanthines and the adenine derivatives. We studied specifically the typical compounds in each category, KW6002 and ZM241385. Both of them are strong binding ligand to $A_{2A}AR$ ($K_i = 12$ n*M* and 1.4 n*M* for KW6002 and ZM241385, respectively) and they are the most well studied ligands in clinical tests and scientific research. There are a lot of experimental data on their ligand binding affinity, selectivity and efficacy. KW6002 has been investigated in several clinical trials for PD,[4,22] for example, its phase III clinical trials on patients were completed in 2009 (not approved by the FDA due to high nonspecific binding).[23] ZM241385 has been widely used as a research tool in scientific studies and is one of the best known chemicals in adenine derivatives. Based on the inactive crystal structure of $A_{2A}AR$-T4 lysosyme (PDB ID: 3EML), we constructed three simulation models, one apo-$A_{2A}AR$ model and two holo-$A_{2A}AR$ models bound with either ZM241385 or KW6002. Our results showed that $L167^{5.28}$ is the antagonist binding specific residue and $N253^{6.55}$ is the most important ZM241385 specific interacting residue.

Our second goal is to study the antagonist induced conformational dynamics of the functional switches in $A_{2A}AR$, thereby suggesting structural indicators for $A_{2A}AR$ antagonism. This could compliment future experimental studies to unravel the molecular mechanism of $A_{2A}AR$ antagonism. $A_{2A}AR$ shares the conserved topology structural fold in the GPCR protein family. It has seven transmembrane helices (TMs) that are connected by three intracellular loops (ICs) and three extracellular loops (ECs).[17] In this structural model, the conformation of the highly conserved motifs and secondary structures of the loops rearrange, switching on and off the receptor. Among them, the "ionic lock," "rotamer toggle switch," and IC2/IC3 are identified to be the characteristic functional switches of proteins in GPCR family. The conformations of these switches sample different states between active and inactive GPCRs.[24–34] In this paper, we identified a series of residues as a part of the ionic lock and rotamer toggle switch for $A_{2A}AR$. We compared the conformational dynamics of these functional characteristic switches among the three structures, two holo-$A_{2A}ARs$ and the apo-$A_{2A}AR$. According to our observation, the ionic lock, rotamer toggle switch and secondary structures of IC2 and IC3, give similar conformations in the two holo-$A_{2A}ARs$, but not apo-$A_{2A}AR$.

METHODS

Structure preparation of $A_{2A}AR$

The missing intracellular loop (IC)3 and extracellular loop (EC)2 were constructed by homo-modeling with Swiss Model.[35] The vasopressin V2 receptor (PDB ID: 2JX4) and β_2AR (PDB ID: 2RH1) were used as templates, respectively. The generated structure was examined by Verify3D[36] and proved to be physical. The Verify3D method evaluates how physical the modeled structures are, by analyzing the compatibility of a three-dimensional atomistic model with its amino acid sequence. It scores structures by comparing the environment of the position and amino acid preferences in this position. The score for a physical structure should be larger than 0 and our resulting structure fits well into this category. Further more, an 1000-step energy minimization was performed by AMBER10 package.[37] The H++[38] was applied to determine the protonation state for titratable groups of the protein at the pH value of 7.0. Missing hydrogen atoms in crystal structure were added by LEaP.[37]

System setup for protein-membrane-solvent model

In VMD,[39] each $A_{2A}AR$ model was inserted into a 100 Å by 100 Å POPC bilayer. POPC molecules with any atom within 5.0 Å of any $A_{2A}AR$ atoms were removed. The $A_{2A}AR$-lipid was solvated by a 50 Å thick water layer in both sides. The full system was neutralized with Cl^- counter-ions with Amber. The final system size was 100 Å by 100 Å by 159 Å, containing ~132,000 atoms.

Construction of apo-$A_{2A}AR$ and KW6002-$A_{2A}AR$

The apo-$A_{2A}AR$ model was obtained by removing the binding antagonist ZM241385 from the crystal structure. KW6002-$A_{2A}AR$ model was prepared with Autodock4.0 package[40] with the ligand set flexible and protein as rigid. KW6002 was docked using the Lamarckian genetic algorithm with local search (GA–LS). The grid number was set to be 60 by 60 by 80 with a grid point spacing of 0.375 Å. The grid was centered on ZM241385, the bound antagonist in the crystal structure, and KW6002 was superimposed on ZM241385 to get the initial position. The grid encompassed the entire ligand binding site and part of the extracellular region. 250 independent GA-LS

trials were performed. For each trial, maximum 27,000 generations were generated on a population of 250 individuals and maximum energy evaluations on 2,500,000 poses were performed. All other parameters were the same as default settings in Autodock4.0. Therefore, there are 2,500,000 poses evaluated in each trial and the one with the highest binding affinity was reported. In the end, 250 poses were generated out of 250 independent trials and further clustered by an RMSD tolerance of 2 Å. Four clusters with members of more than 10 were gathered (Supporting Information Fig. S1). To get the most probable binding mode, the one with lowest binding energy score in each of the four clusters were chosen to perform further MD simulations. The binding modes were further determined with MD simulations and detailed binding energy calculations (Supporting Information Fig. S2 and Table S1).

Force field parameters

MD simulations were performed by NAMD package[41] with Amber force field FF99SB for the protein and GAFF for antagonists and POPC membrane molecules. Atomic charges of antagonists were derived from R.E.D,[42] in which structure optimizations and electrostatic potential calculations were taken with Gaussian03[43] at the level of HF/6–31G*. The partial charges were fitted using RESP algorithm and atom types were allocated by ANTECHAMBER module. The atom charge and atom type of POPC was taken from the paper by Wang and Duan.[44]

Protocol of molecular dynamics simulation

First, the system was relaxed by a combined energy minimization and MD simulation scheme. Keeping the protein, antagonist, POPC membrane molecules and crystal water fixed with a force constant of 2 kcal/(mol × Å^2), we then relaxed the solvent using 10,000-step energy minimization followed by 500,000-step NPγT MD simulation. After that, the constrains on POPC molecules was removed and the whole system was relaxed by another 10,000-step energy minimization and 500,000-step NPγT MD simulation. The protein, antagonist, and crystal water molecules were relaxed using the same protocol.

The whole system was heated gradually to 310 K by Langevin dynamics with a damping coefficient of 1.0 ps^{-1}. NPγT ensemble was used, with the surface tension set to 60 mN/m and the pressure set to 1.01325 bar. The Langevin piston Nosé-Hoover method was used to control the pressure,[45] with damping and oscillation time scales of Langevin piston set as 50 and 100 fs, respectively. Covalent bonds involving hydrogen were restrained by the SHAKE algorithm.[46] The short-ranged nonbonded interaction was switched off gradually from 10 Å to 12 Å. The PME method[47] was applied to treat long-range electrostatic interactions, and the grid size is 120 Å by 120 Å by 180Å. A multiple-time-step scheme was used with covalent forces evaluated every 1.0 fs. For the first 10 ns simulation, a multiple time step of 1.0 fs for short-range nonbonded forces, and 2.0 fs for long-range electrostatic forces were used; and 2.0 fs for short-range nonbonded forces, 4 fs for long-range electrostatic forces was used in the following simulation.

Binding energy decomposition

Binding energies between ligands (ZM241385 or KW6002) and protein-lipid molecules were calculated and decomposed on each residue of protein and lipid membrane with the MM-GBSA module in Amber.[37] The calculations were performed according to the thermodynamic circle shown in Supporting Information Figure S3, and the binding energy is calculated by:

$$\Delta G_{\text{Bind}}^{\text{Solve}} = \Delta G_{\text{Bind}}^{\text{Gas}} + \Delta G_{\text{Complex}}^{\text{Solve}} - \left(\Delta G_{\text{Ligand}}^{\text{Solve}} + \Delta G_{\text{Protein-lipid}}^{\text{Solve}}\right) \quad (1)$$

The $\Delta G_{\text{Bind}}^{\text{Gas}}$ term consists of the gas phase electrostatic interactions and van der Waals interactions (between ligand and protein-lipid in the complex), and the internal energy variations (between the complex and isolated molecules, which includes bond, angle and torsion angle interactions).

$$\Delta G_{\text{Bind}}^{\text{Gas}} = \Delta G_{\text{elec}}^{\text{Gas}} + \Delta G_{\text{vdW}}^{\text{Gas}} + \Delta G_{\text{intra}}^{\text{Gas}} \quad (2)$$

The solvation free energies, ΔG^{Solve}, is composed of the electrostatics interaction difference between solvent environment ($\varepsilon = 78.5$) and gas phase ($\varepsilon = 0$), and the nonpolar contributions.

$$\Delta G^{\text{Solve}} = \Delta G_{\in=78.5}^{\text{elec}} - \Delta G_{\in=0}^{\text{elec}} + \Delta G_{\text{np .solve}} \quad (3)$$

The electrostatic part is calculated with the MM-GBSA model. The nonpolar contribution arises from the sum of cavity term and a solute-solvent van der Waals term. It is assumed to be proportional to the solvent accessible surface area (SASA), and a surface tension of $\gamma = 0.0072$ kcal/mol/Å^2 is used.

$$\Delta G_{\text{np .solve}} = \gamma \text{ SASA} \quad (4)$$

The energy terms were averaged over 1000 frames extracted from each 10 ns trajectory in the MD simulations. Snapshots of 40 to 50 ns, 90 to 100 ns, 140 to 150 ns, 190 to 200 ns, 240 to 250 ns, 290 to 300 ns, 340 to

350 ns and 390 to 400 ns were calculated, respectively. The POPC lipid molecules were also included in the energy calculation, so as to find out possible interactions between POPC molecules and the ligand. In the energy decomposition, the contributions of each term were decomposed to each residue of the protein and lipid. The binding mode selection of KW6002 was performed in the same way, except that we did not consider the lipid molecules in the calculations. Since we mainly focused on which residues contribute greatly to ligand binding, we did not consider entropy contribution in this work.[48]

Analysis protocols

The root-mean-square deviation (RMSD), distance between specific atom pairs, dihedral angles of residues, and hydrogen bonding interactions were analyzed by PTRAJ module of AMBER10. RMSD of protein and ligands were used to evaluate the convergence of the simulation (Supporting Information Figs. S4 and S5). DSSP algorithm[49] was applied to assign the secondary structure content of IC2 and IC3 along MD simulation. We also clustered the structures with MMTSB[50] so as to get the most representative conformations during the rotamer toggle switching process in apo-A_{2A}AR with respect to RMSD of residues 242–250 and residue T88$^{3.36}$. Individual structures with lowest RMSD to the most populated centroid were taken as the most representative ones.

RESULTS AND DISCUSSIONS

Determining KW6002 binding mode via docking and binding energy decomposition

To determine the binding site of the ligand, we first predicted the binding mode between KW6002 and A_{2A}AR by AutoDock,[40] and then selected typical binding mode from short MD simulations and binding energy decomposition calculations. We performed 250 docking trials, in which 2,500,000 poses were evaluated and the highest binding affinity one was recorded in each trial. Thus the 250 binding modes were picked out from 250 $\times$ 2,500,000 poses, through 250 independent runs. Since the docking program did not consider the flexibility of the protein structure, we chose four most representative structures out of the resulted 250 binding modes [Supporting Information Figs. S1 and S2(A,B)] and performed MD simulations on them to achieve equilibrium [Supporting Information Fig. S2(C,D)]. Binding energies between the KW6002 and protein were calculated with MM-GBSA in every 10 ps during the simulation, and further decomposed into terms of contributions on a per-residue basis for each binding mode. Residues such as F168$^{5.29}$, E169$^{5.30}$, W246$^{6.48}$, L249$^{6.51}$, H250$^{6.52}$, N253$^{6.55}$, L267$^{7.32}$, M270$^{7.35}$, and I274$^{7.39}$ were reported to be important for antagonist binding in experiments[17] (residues are labeled according to the Ballesteros-Weinstein residue numbering method,[51] explained in the Supporting Information). As shown in Figure 1, for the binding mode of KW-2, KW6002 interacted strongly with those residues and the total binding affinity was also the strongest [$-$23.09 kcal/mol in KW-2, versus $-$20.04 kcal/mol, $-$21.12 kcal/mol and $-$20.51 kcal/mol in KW-1, KW-3, and KW-5, respectively. See Supporting Information Table S1 and Fig. S2(C,D)]. Since KW6002 does not have hydrophilic group, it is understandable that a slight penalty instead of favorable interactions were found between KW6002 and E169$^{5.30}$. Therefore, we choose KW-2 as the binding mode for further MD simulation.

Identified key antagonist-binding residues in A_{2A}AR via interaction energy analysis

To identify important A_{2A}AR residues that interact with ZM241385/KW6002, we analyze interactions between A_{2A}AR and the antagonist by averaging the binding energy over 8 trajectories for each holo-A_{2A}AR. Residues with interactions stronger than 0.5 kcal/mol and interacting residues from the ionic lock and rotamer toggle switch were shown in Figure 2. The detailed decompositions with standard deviation were shown in Supporting Information Table S2. POPC lipid molecules were also included in the calculation, but no strong interactions between ligands and lipids were found. Among the residues reported to be important for antagonist binding from experiments,[17] both ligands interacted with F168$^{5.29}$, W246$^{6.48}$, L249$^{6.51}$, H250$^{6.52}$, L267$^{7.32}$, M270$^{7.35}$, and I274$^{7.39}$. Also, they interacted with I66$^{2.64}$, V84$^{3.32}$, L85$^{3.33}$, T88$^{3.36}$, and L167$^{5.28}$. However, L167$^{5.28}$ was not found interacting with the agonist.[18,19,21] Moreover, specific binding between the two ligands and A_{2A}AR were observed: ZM241385 specifically bound to S67$^{2.65}$, M177$^{5.38}$, and N253$^{6.55}$, while KW6002 specifically interacted with F62$^{2.60}$, A81$^{3.29}$, and H264$^{7.29}$. With strong electrostatic interactions, N253$^{6.55}$ contributed the most to the total binding energy among all other ligand specific interacting residues, which could be the reason why ZM241385 shows in experiments higher binding affinity than KW6002 (K_i = 1.4 n*M* vs. K_i = 12 n*M*). The F62$^{2.60}$, A81$^{3.29}$, and H264$^{7.29}$ interacted with KW6002 mainly via Van de Waals interactions. The relative positions of the interacting residues were illustrated in Figure 2. Antagonist derivatives, with improved binding affinity to L167$^{5.28}$ and residues specifically binding to ZM241385 (especially N253$^{6.55}$), could trigger A_{2A}AR inactivation.

Antagonist binding induced ionic-lock breakage in holo-A_{2A}ARs

The ionic lock was believed to be important in the inactive state of GPCR,[17,24,30,52,53] but it was broken

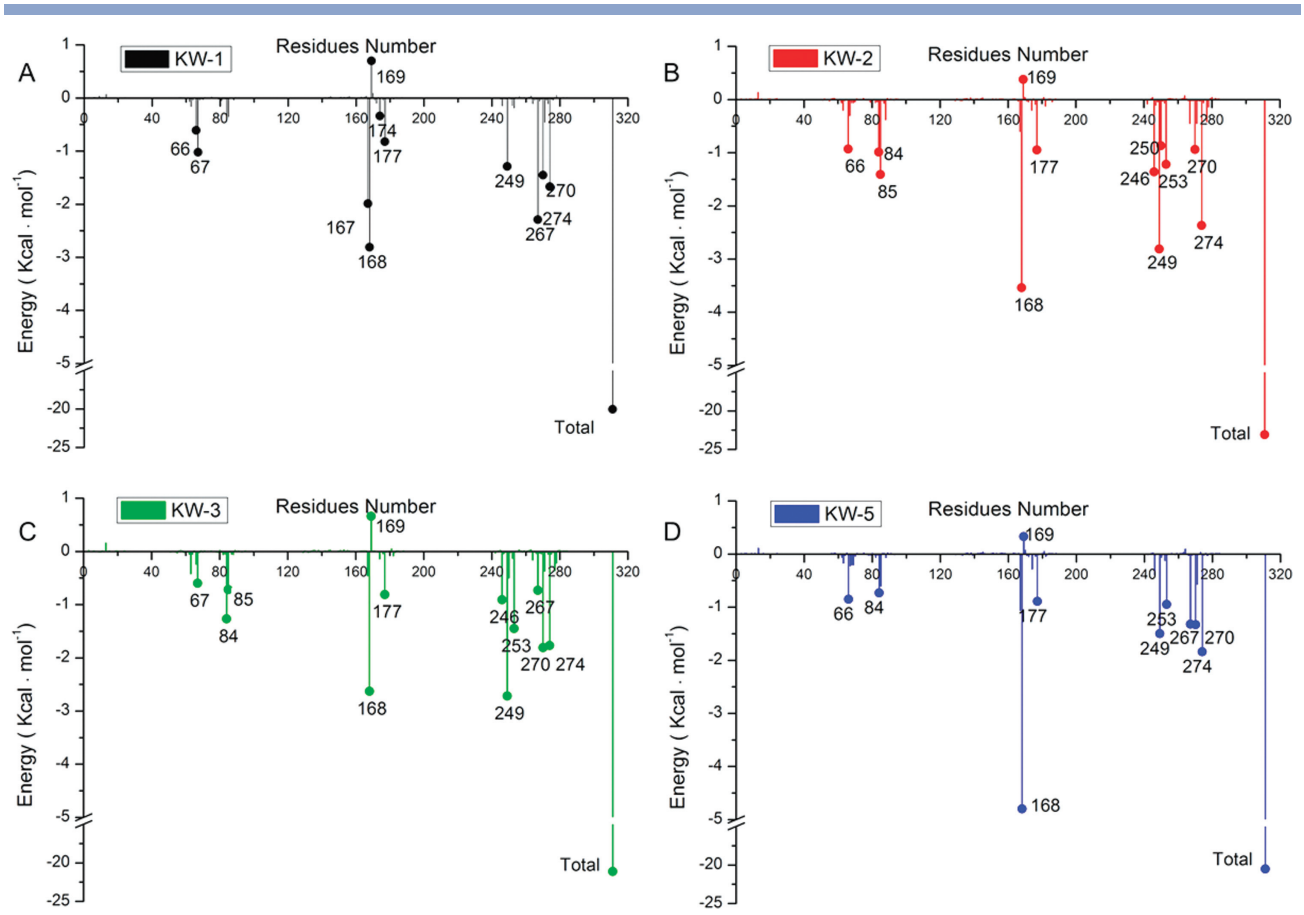

Figure 1

Binding energy decompositions of the four selected binding modes between KW6002 and A_{2A}AR. The total binding energy was decomposed on each residue of A_{2A}AR and interactions greater than 0.5 kcal/mole were illustrated. (**A–D**) Interaction energy decompositions of binding mode KW-1, KW-2, KW-3, and KW-5, respectively.

in the crystal structure of the inactive A_{2A}AR.[17] Contributed from hydrogen bonding and electrostatic interactions, the ionic lock in A_{2A}AR is composed of a set of salt bridge interactions between the intracellular ends of TM3 and TM6. The ionic lock was first reported as stabilizing the inactive states in rhodopsin, the most widely studied GPCR.[24] Mutagenesis, electron paramagnetic resonance spectra, and ultraviolet-visible absorption spectral studies on rhodopsin suggested that in the inactive state, residues in the ionic lock were closer to each other and the lock formed; whereas in the active state, they were farther apart and the lock broke.[25,26] Other GPCRs were also believed to have such an ionic lock in their inactive states.[17,24,30,52,53] However, the three newly resolved GPCR structures (A_{2A}AR-antagonist: PDB ID: 3EML,[17] β_1AR: PDB ID: 2VT4[30], and β_2AR: PDB ID: 2RH1, 3D4S, and 2R4R[53,54]) did not have such ionic lock, even though they have been believed to be inactive. MD simulations showed that β_2AR equilibrated between conformations of lock formed and broken, regardless of the existence of co-crystallized ligands.[55] We thus addressed the residues involved in the ionic lock, and checked their conformational states in A_{2A}AR during the simulation.

Our analyses on hydrogen bond formations and heavy atom distances suggested that the ionic lock in apo-A_{2A}AR equilibrated between formation and breakage, while it stayed broken in the two holo-A_{2A}ARs. According to the crystal structure, the ionic lock of rhodopsin consists of $D^{3.49}$ or $R^{3.50}$ from the highly conserved (D/E)RY motif and $E^{6.30}$ or $T^{6.34}$ in TM6.[24] Also, $R^{3.50}$ and $E^{6.30}$ were frequently identified as residues comprising the ionic lock.[17,20,55] Therefore, we first analyzed hydrogen bond interactions of $R102^{3.50}$ and $E228^{6.30}$, so as to find residues involved in the ionic lock of A_{2A}AR. $R102^{3.50}$ did not form hydrogen bond with residues in TM6 of holo-A_{2A}ARs (lifetime percentage <10% and hydrogen bond occupancy <40%), whereas hydrogen bonds between $R102^{3.50}$ and $E228^{6.30}$ or $H230^{6.32}$ were observed in apo-A_{2A}AR. $E228^{6.30}$ also formed hydrogen bond with $R107^{3.55}$ in addition to $R102^{3.50}$ in apo-A_{2A}AR (Supporting Information Table S3). We examined

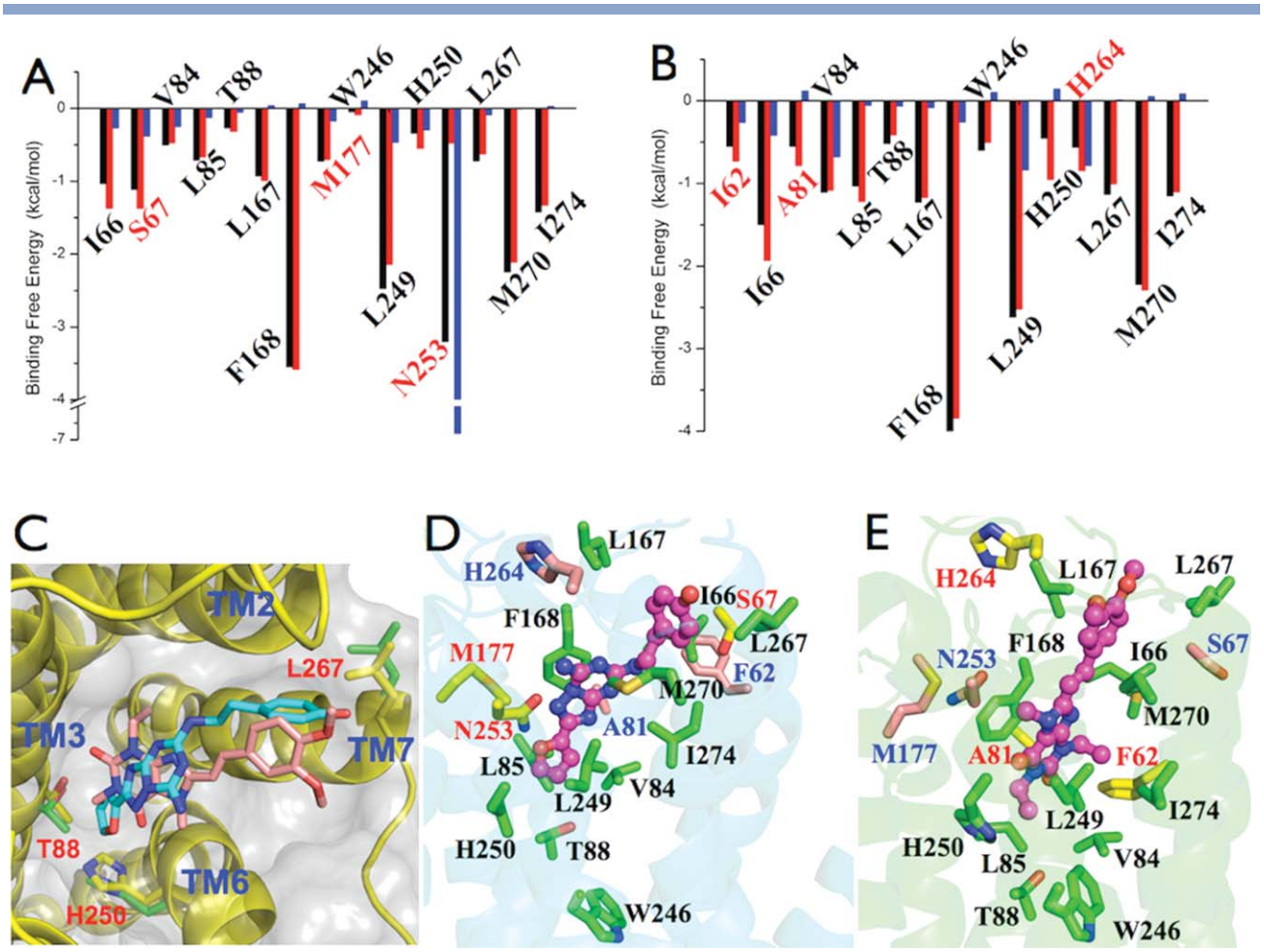

Figure 2

Protein-ligand interactions of ZM241385-A_{2A}AR and KW6002-A_{2A}AR. (**A**) Binding energy decomposition of ZM241385-A_{2A}AR. (**B**) Binding energy decomposition in KW6002-A_{2A}AR. Electrostatic interactions were shown in blue columns, vdW interactions in red columns and total interactions in black columns. Residues interacting with both ZM241385 and KW6002 were labeled in black; ligand specific interactions were labeled in red. (**C**) Overview of the protein-ligand interactions, ZM241385 and KW6002 occupied similar special position in the binding pocket. A_{2A}AR was shown in yellow cartoon and gray surface; ZM241385 shown in cyan sticks; KW6002 shown in pink sticks; residues in ZM241385-A_{2A}AR shown in green sticks; residues in KW6002-A_{2A}AR shown in yellow sticks. (**D**) Illustration of interaction in ZM241385-A_{2A}AR. A_{2A}AR was shown in cyan cartoon; ZM241385 in magenta stick-spheres; residues interacting with both ZM241385 and KW6002 shown in green sticks with black labels; residues only interacting with ZM241385 shown in yellow sticks with red labels; residues only interacting with KW6002 shown in pink sticks with blue labels. (**E**) Interaction illustration of KW6002-A_{2A}AR. A_{2A}AR was shown in green cartoon; KW6002 in magenta stick-spheres; residues interacting with both ligands shown in green sticks with black labels; residues interacting with KW6002 only shown in yellow sticks with red labels; residues interacting with ZM241385 only shown in pink sticks with blue labels. [Color figure can be viewed in the online issue, which is available at wileyonlinelibrary.com.]

the ionic lock stability by calculating distances between atoms of $R102^{3.50}$–$E228^{6.30}$, $R107^{3.55}$–$E228^{6.30}$, and $R102^{3.50}$–$H230^{6.32}$. Figure 3 showed the time series of the closest distance between these residue pairs. Apo-A_{2A}AR fluctuated between conformations with formed and broken lock. The salt bridge between $R102^{3.50}$ and $E228^{6.30}$ formed and maintained within the first 160 ns. Then the salt bridge between $R107^{3.55}$ and $E228^{6.30}$ formed from 190 ns to 240 ns. In the rest of the simulation, $R102^{3.50}$ hydrogen bonded with $H230^{6.32}$. However, in holo-A_{2A}ARs the ionic lock was far less frequently formed and was quite instable, e.g. the ionic lock of ZM241385-A_{2A}AR completely broke after 250 ns. Considering the time series of ionic lock distances, we selected snapshots at 50 ns, 200 ns, and 300 ns to show the orientations and motions of TM3 and TM6 (Supporting Information Fig. S6). The larger ionic lock distances in holo-A_{2A}ARs indicated that antagonist binding weakened the lock and changed the relative position between TM3 and TM6.

$T88^{3.36}$/$F242^{6.44}$/$W246^{6.48}$ functioned as the rotamer toggle switch in A_{2A}AR

Rotamer toggle switch was another structural element that could switch the GPCRs between active and inactive states by changing their χ1 rotamers (measured by the

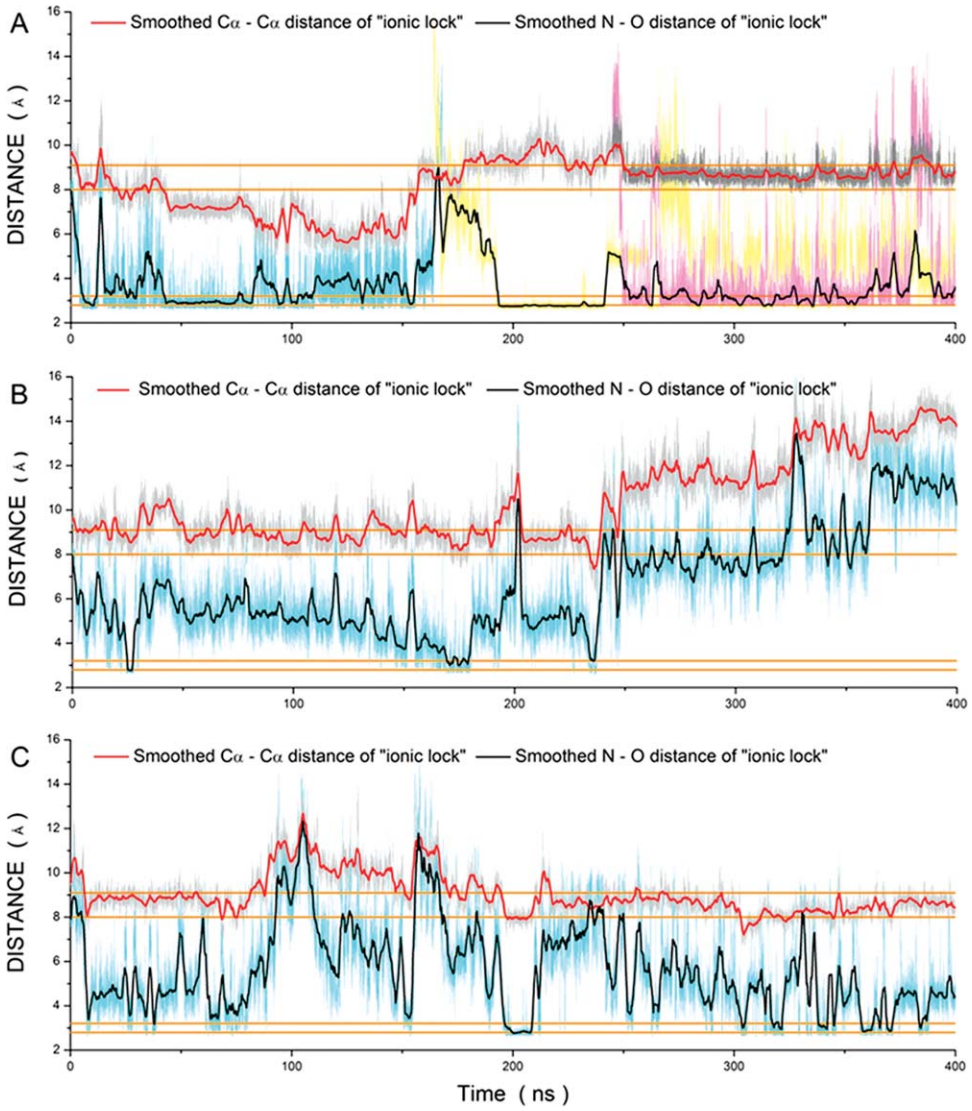

Figure 3

Ionic lock time series of apo-A_{2A}AR and holo-A_{2A}ARs, assessed by both the side chain and backbone distances between residues involved. The smoothed side chain distances (N-O distances) were shown in black and backbone distances (Cα-Cα distances) in red. The corresponding distances observed in two inactive rhodopsin crystal structures (PDB ID: 1U19 and 1L9H) were indicated by orange lines. (**A**) Ionic lock of apo-A_{2A}AR was evaluated by the closest side chain and backbone distances between residue pairs of $R102^{3.50}$–$E228^{6.30}$, $R107^{3.55}$–$E228^{6.30}$, and $R102^{3.50}$–$H230^{6.32}$. The nearest N-O distance between $R102^{3.50}$ and $E228^{6.30}$ was shown in cyan; Cα-Cα distance in gray; the nearest N-O distance between $R107^{3.55}$ and $E228^{6.30}$ in light yellow; the nearest N-O distance between $R102^{3.50}$ and $H230^{6.32}$ in light pink; and Cα-Cα distance in dark gray. (**B**) Ionic lock in ZM241385-A_{2A}AR assessed by distances between $R102^{3.50}$ and $E228^{6.30}$. The nearest N-O distance was shown in cyan, while the Cα-Cα distance was shown in gray. (**C**) Ionic lock of KW6002-A_{2A}AR assessed by distances between $R102^{3.50}$ and $E228^{6.30}$. The nearest N-O distance was shown in cyan, and the Cα-Cα distance was shown in gray. [Color figure can be viewed in the online issue, which is available at wileyonlinelibrary.com.]

N-C_α-C_β-C_γ torsion angle) in response to ligand binding.[29] It was proposed that the rotamer toggle switch was composed of $W^{6.48}$ in the highly conserved WXP motif and other residues spatially adjacent to $W^{6.48}$, and these residues rearranged their rotameric states accordingly. Since both the ligand contact area and residues near $W^{6.48}$ differed among different GPCR subtypes, the components of this rotamer toggle switch were expected to be different. So far, rotamer toggle switches with both $W^{6.48}$/$F^{3.36}$ in CB1 receptor[27] and $T^{6.47}$/$W^{6.48}$/$F^{6.49}$ from β_2AR[28] have been reported. Other residues were also reported to restrain the rotation of $W^{6.48}$, which functioned as parts of the rotamer toggle switch. To identify the rotamer toggle switch in A_{2A}AR, we analyzed the side chain χ1 rotation states of all the reported residues as well as those spatially close to $W246^{6.48}$ in both TM3 and TM6.

$T88^{3.36}$/$F242^{6.44}$/$W246^{6.48}$ was identified as the rotamer toggle switch in A_{2A}AR, and it adopted the same rotation states in both holo-A_{2A}ARs but a different state in apo-A_{2A}AR. $W246^{6.48}$ remained in gauche- states (χ1 near

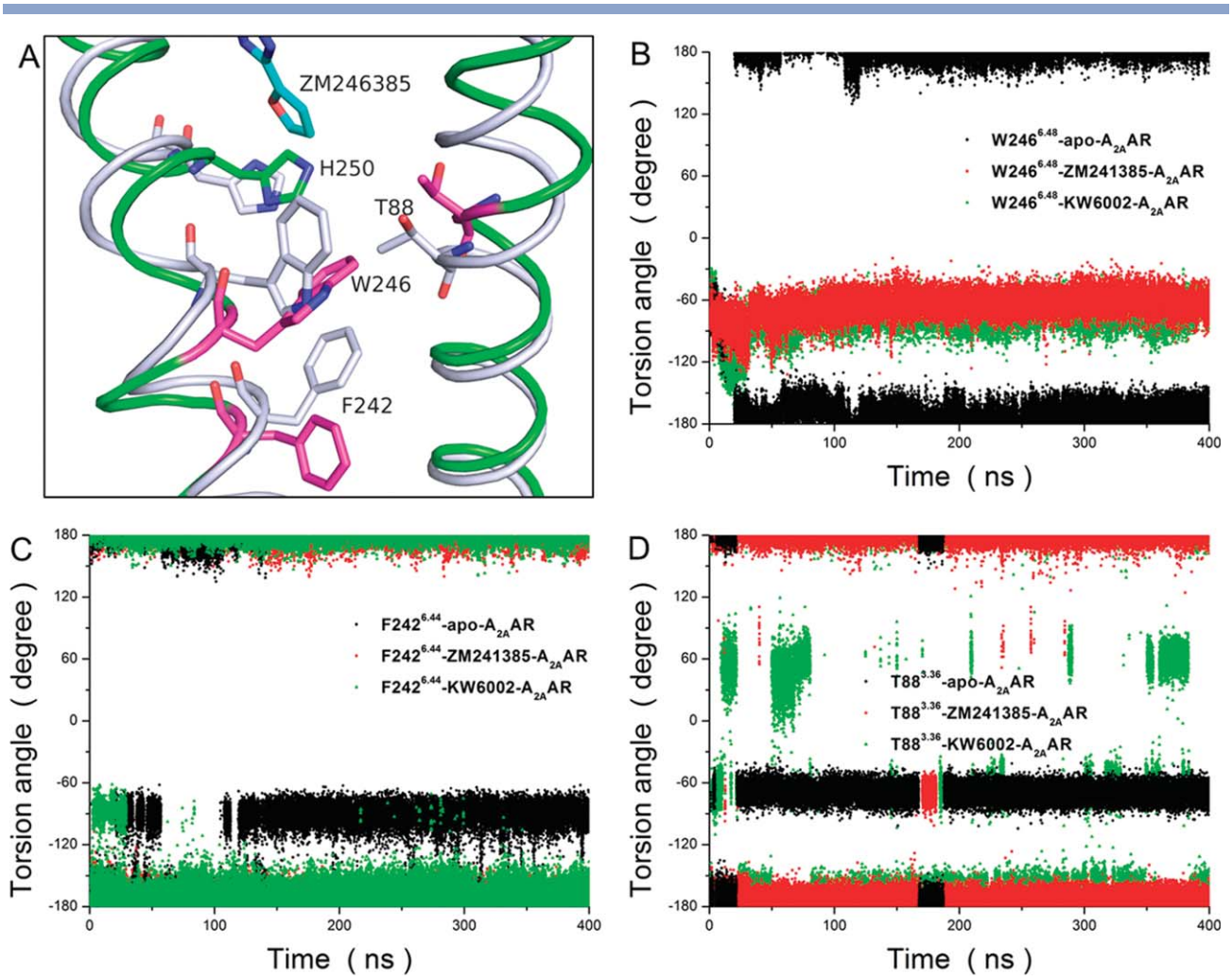

Figure 4

Side chain conformations and rotamer changes of $T88^{3.36}$/$F242^{6.44}$/$W246^{6.48}$ and $H250^{6.52}$ in A_{2A}ARs (gauche+, $\chi1$ near 60°; gauche−, $\chi1$ near −60°; and trans, $\chi1$ near ± 180°). (**A**) Conformations of the $T88^{3.36}$/$F242^{6.44}$/$W246^{6.48}$ and $H250^{6.52}$. Apo-A_{2A}AR at 21.8 ns was superimposed with the crystal structure. The apo-A_{2A}AR was shown in green cartoon; the crystal structure was shown in gray cartoon; related residues and ZM241385 indicated in sticks. Residues of different rotation states were highlighted in pink and ZM241385 in cyan. (**B**) $W246^{6.48}$ switched to a trans conformation in apo-A_{2A}AR, whereas it remained gauche- in holo-A_{2A}ARs. (**C**) $F242^{6.44}$, which was reported to flank rotation of $W246^{6.48}$, sampled frequently as gauche- in apo-A_{2A}AR, whereas in holo-A_{2A}AR it remained in trans. (**D**) $T88^{3.36}$ frequently sampled gauche- in apo-A_{2A}AR, whereas in holo-A_{2A}ARs it mostly adopted trans conformations. [Color figure can be viewed in the online issue, which is available at wileyonlinelibrary.com.]

−60°) and seated almost parallel to TM3 and TM6 in holo-A_{2A}ARs, while in apo-A_{2A}AR it shifted to trans ($\chi1$ near ±180°) and plumbed with these two TMs [Fig. 4(A,B)]. Among all other reported residues, $T88^{3.36}$ and $F242^{6.44}$ took trans rotamer in holo-A_{2A}ARs, but both of them switched to gauche- in apo-A_{2A}AR [Fig. 4(A,C,D)]. $H250^{6.52}$ sampled trans conformation in both apo-A_{2A}AR and holo-A_{2A}ARs and functioned on rotamer switching of $W246^{6.48}$ via hydrogen bond interactions (Supporting Information Table S4). Based on the rotation time series [Fig. 4(B–D)], we further clustered the snapshots during the switching process in apo-A_{2A}AR. The representative structures were shown in Figure 5. First, the aromatic ring of $W246^{6.48}$ slipped down as a rigid body nearly perpendicular to TM3 and TM6 [Fig. 5(A)]. Then $H250^{6.52}$ moved close to $W246^{6.48}$ and resulted in conversion of gauche- $W246^{6.48}$ into trans conformation [Fig. 5(B)]. To accommodate the rotation of $W246^{6.48}$, $F242^{6.44}$ rotated to gauche- and further flanked $W246^{6.48}$ in the trans state [Fig. 5(C)]. Finally, $T88^{3.36}$ switched to gauche- so as to reduce conformational conflicts with the new state of $W246^{6.48}$ [Fig. 5(D)]. Thus, $T88^{3.36}$/$F242^{6.44}$/$W246^{6.48}$ acted as the rotamer toggle switch in A_{2A}AR and adopted different rotation states between apo and holo structures.

Antagonist binding changed the secondary structure of IC2 and IC3

For all GPCRs, IC2 (TM3-IC2-TM4) and IC3 (TM5-IC3-TM6) were believed to be "switch regions" that

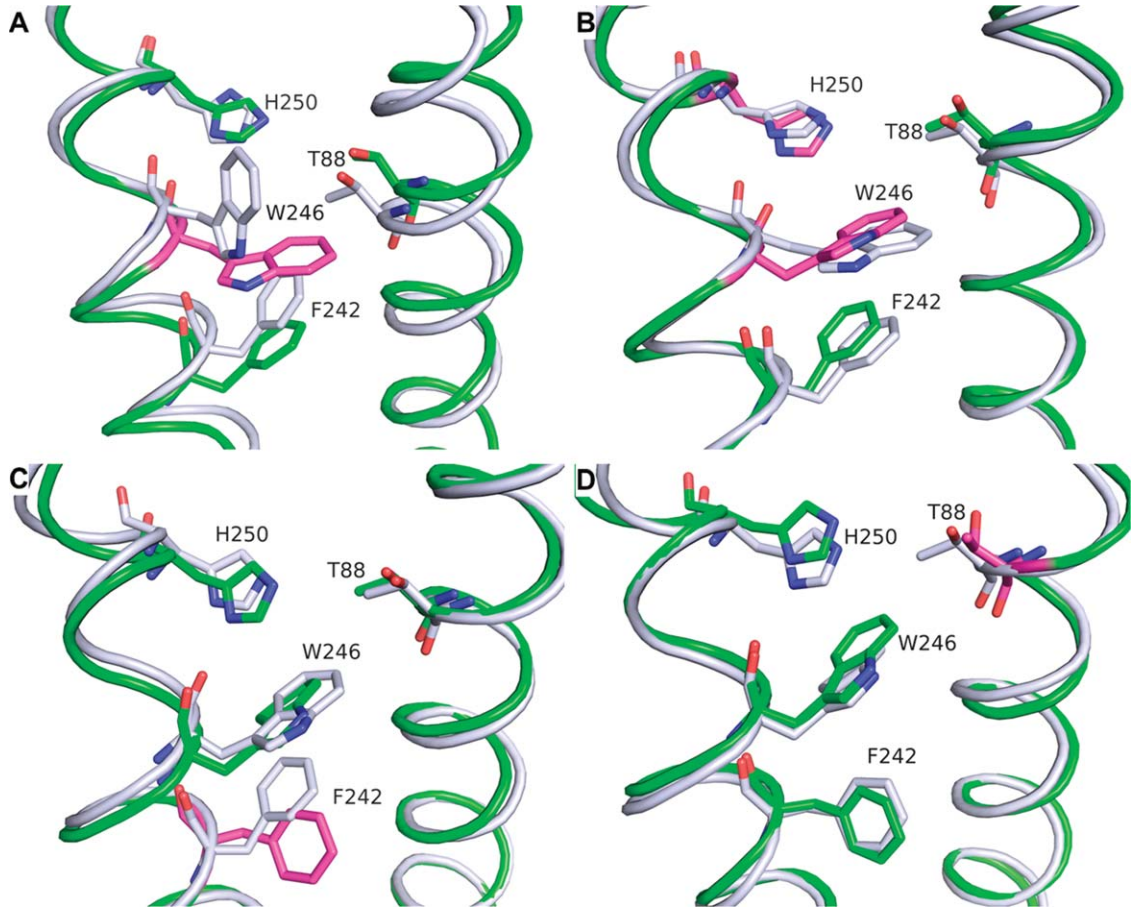

Figure 5

Side chain rotameric switches of $T88^{3.36}$/$F242^{6.44}$/$W246^{6.48}$ and rigid body motion of $H250^{6.52}$ in apo-A_{2A}AR. (**A**) At approximately 19.5 ns, $W246^{6.48}$ slipped down as a rigid body. The MD snapshot was shown in green cartoon and sticks, and the residues involved in rotamer changes were highlighted in pink. The crystal structure was used for reference and shown in gray. (**B**) At approximately 19.9 ns, $W246^{6.48}$ rotated to the trans conformation. The structure at about 19.5 ns was used for reference and shown in gray. (**C**) At approximately 20.7 ns, $F242^{6.44}$ rotated to gauche-. The structure at 19.9 ns was used for reference and shown in gray. (**D**) At approximately 21.8 ns, $T88^{3.36}$ switched to gauche-. The structure at 20.7 ns was used for reference and shown in gray. [Color figure can be viewed in the online issue, which is available at wileyonlinelibrary.com.]

could alter the equilibrium between active and inactive states. It was proposed that IC2 were responsible for the binding affinity[30,31] and IC3 for selectivity[32,33] of proteins that GPCR interacting with, e.g. G proteins. Further more, the change in secondary structures in their IC2 and IC3 could indicate the activation/inactivation of GPCR. The formation of α-helical IC2 might restrain GPCRs in their inactive states and weakened their binding to G proteins.[31,34] The α-helical IC3 was suggested to be crucial for interactions between GPCR and the G proteins, and further activating G proteins.[56,57] For IC3, the first 12 residues adjacent to TM5 were believed to be important for G protein activation, and the subsequent nine residues could alter the binding selectivity between GPCRs and G proteins.[57] Furthermore, among recently resolved crystal structures, different secondary structures of the two loops were observed.[17,24,29,30,53,54,58–60] Since both the ionic lock and rotamer toggle switch behaved differently between apo-A_{2A}AR and holo-A_{2A}ARs, we further analyzed the secondary structures of IC2 and IC3 to characterize the conformational differences induced by antagonist binding.

The secondary structure analysis suggested that apo-A_{2A}AR preferred α-helical IC2 and flexible IC3; whereas in holo-A_{2A}ARs, an irregular IC2 and a short α-helical or 3_{10}-helical IC3 were more frequently observed (Fig. 6 and Supporting Information Fig. S7). We compared the secondary structures of IC2 and IC3 between the two holo structures and between holo and apo structures. In apo-A_{2A}AR, IC2 adopted α-helix, while in holo-A_{2A}ARs it frequently behaved as irregular loops [Fig. 6(A–C) and cartoons shown in Supporting Information Fig. S7]. For IC3, though the initial structure from homo-model was a long α-helix, it quickly transited to irregular loops and remained flexible in apo-A_{2A}AR, whereas a short α-helix (or 3_{10}-helix) was formed in holo-A_{2A}ARs [Fig. 6(D–F)].

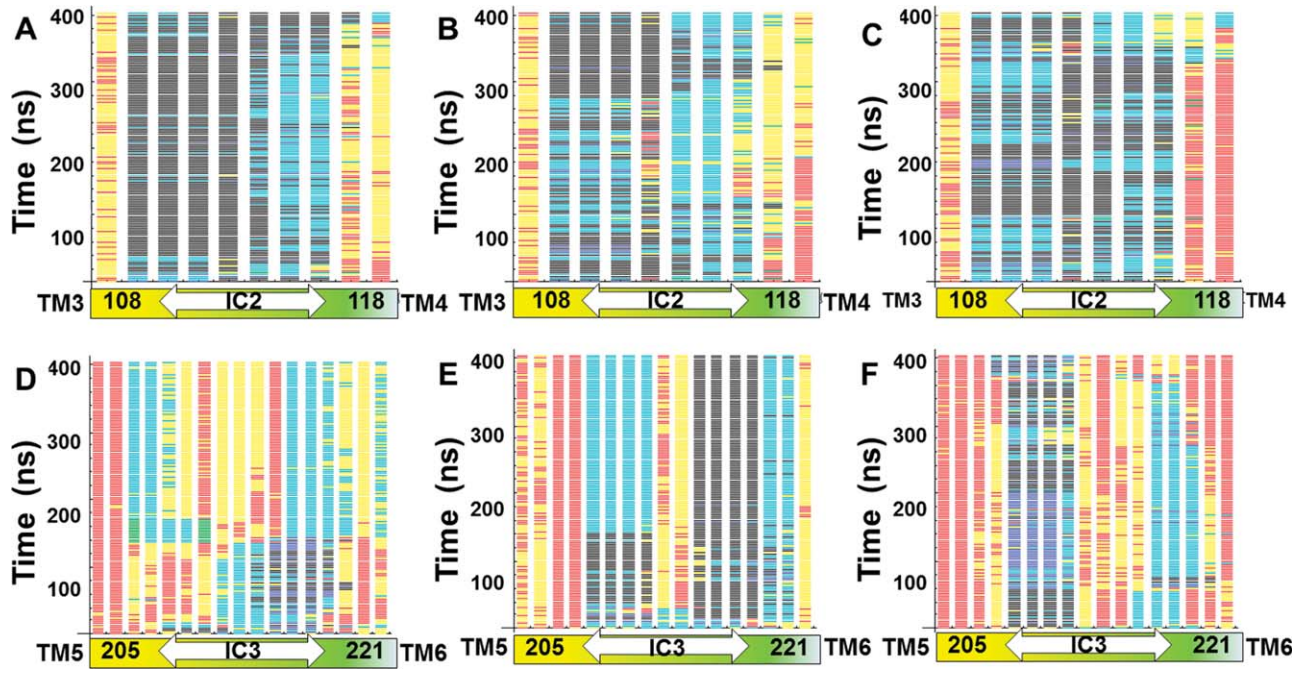

Figure 6

Secondary structure contents of IC2 and IC3 in the apo-A_{2A}AR and holo-A_{2A}ARs during MD simulations. Alpha helix was colored in black, 3_{10}-helix in blue, extended strand in beta ladder or isolated beta-bridge in green, hydrogen bonded turn in cyan, bend in yellow, and coil in red. Hydrogen bonded turns, bends and coils were called loops. (**A**) IC2 of apo-A_{2A}AR preferred a short α-helix. In holo-A_{2A}ARs, ZM241385-A_{2A}AR (**B**) and KW6002-A_{2A}AR (**C**), IC2 frequently exhibited irregular loops. (**D**) In apo-A_{2A}AR, IC3 adopted flexible irregular loops, and a short α-helix or 3_{10}-helix was formed in holo-A_{2A}ARs, ZM241385-A_{2A}AR (**E**) and KW6002-A_{2A}AR (**F**). [Color figure can be viewed in the online issue, which is available at wileyonlinelibrary.com.]

To sum up, antagonist binding in A_{2A}AR induced the secondary structure adjustments in IC2 and IC3. The conformational change of IC2 and IC3 in A_{2A}AR could become a dynamic indicator for A_{2A}AR activation/inactivation in experimental studies.

CONCLUSION

In this study, the binding of two distinct antagonists to A_{2A}AR and the antagonist induced conformational dynamics were studied. We first investigated the antagonist binding and identified the key antagonist binding residues by comparing the two holo-A_{2A}ARs. Besides residues interacting to both antagonists, $S67^{2.65}$, $M177^{5.38}$, and $N253^{6.55}$ specifically bound with ZM241385, while unique interactions between KW6002 and $F62^{2.60}$, $A81^{3.29}$, and $H264^{7.29}$ were observed. Among the ZM241385 specific interacting residues, $N253^{6.55}$ contributes the most to the total binding energy, which could be responsible for higher relative binding affinity of ZM241385 comparing with KW6002. Moreover, antagonist and agonist binding to A_{2A}AR are different: both ZM241385 and KW6002 bound with $L167^{5.28}$, which was not reported in agonist binding. We thus propose that antagonist derivatives, with improved $L167^{5.28}$ and $N253^{6.55}$ binding affinity, might enhance A_{2A}AR inactivation.

Furthermore, we demonstrated the antagonist induced conformational dynamics of the characteristic functional switches: ionic lock, rotamer toggle switch and IC2/IC3, by comparing the two holo-A_{2A}ARs and apo-A_{2A}AR. Compositions of the ionic lock and rotamer toggle switch in A_{2A}AR were identified and important structural conformation differences were found between apo-A_{2A}AR and holo-A_{2A}ARs. Tight ionic lock between TM3 and TM6 frequently formed in apo-A_{2A}AR, while the ionic lock in both of the two holo-A_{2A}ARs was mostly broken and in ZM241385-A_{2A}AR was completely broken throughout the simulation. $T88^{3.36}$/$F242^{6.44}$/$W246^{6.48}$ functioned as the rotamer toggle switch and adopted the same χ1 rotation states in both holo structures, but gave different conformation in apo-A_{2A}AR. Apo-A_{2A}AR adopted α-helical IC2 and flexible IC3, while both ZM241385-A_{2A}AR and KW6002-A_{2A}AR showed flexible IC2 and α-helical IC3. Similar conformational dynamics of the functional switches in both holo-A2AARs are consistent with the experimental findings that both KW6002 and ZM241385 have therapeutic effect.[2] The antagonism dynamic behaviors of these switches could be used as monitors of A_{2A}AR activation/inactivation transition and thus help to unravel the functional mechanisms of A_{2A}AR antagonism.

ACKNOWLEDGMENTS

The authors thank Prof. John Z.H. Zhang (New York University and East China Normal University) and Prof. Ye Mei (East China Normal University) for helpful discussions and suggestions on methods to perform the MD simulation and data analysis.

REFERENCES

1. Hanson MA, Stevens RC. Discovery of new GPCR biology: one receptor structure at a time. Structure 2009;17:8–14.
2. Zezula J, Freissmuth M. The A(2A)-adenosine receptor: a GPCR with unique features? Br J Pharmacol 2008;153:S184–S190.
3. Cieslak M, Komoszynski M, Wojtczak A. Adenosine A(2A) receptors in Parkinson's disease treatment. Purinergic Signal 2008;4:305–312.
4. Hauser RA, Hubble JP, Truong DD, Grp IU-S. Randomized trial of the adenosine A(2A) receptor antagonist istradefylline in advanced PD. Neurology 2003;61:297–303.
5. Salamone JD. Preladenant, a novel adenosine A(2A) receptor antagonist for the potential treatment of parkinsonism and other disorders. Idrugs 2010;13:723–731.
6. Blum D, Hourez R, Galas MC, Popoli P, Schiffmann SN. Adenosine receptors and Huntington's disease: implications for pathogenesis and therapeutics. Lancet Neurol 2003;2:366–374.
7. Jones PA, Smith RA, Stone TW. Protection against hippocampal kainate excitotoxicity by intracerebral administration of an adenosine A2A receptor antagonist. Brain Res 1998;800:328–335.
8. Monopoli A, Lozza G, Forlani A, Mattavelli A, Ongini E. Blockade of adenosine A2A receptors by SCH 58261 results in neuroprotective effects in cerebral ischaemia in rats. Neuroreport 1998;9:3955–3959.
9. Ohta A GE, Prasad SJ, Ronchese F, Lukashev D,Wong MK et al. A2A adenosine receptor protects tumors from antitumor T cells. Proc Natl Acad Sci USA 2006;103:13132–13137.
10. Ferre S, Fredholm BB, Morelli M, Popoli P, Fuxe K. Adenosine-dopamine receptor-receptor interactions as an integrative mechanism in the basal ganglia. Trends Neurosci 1997;20:482–487.
11. Ferre S, Karcz-Kubicha M, Hope BT, Popoli P, Burgueno J, Gutierrez MA, Casado V, Fuxe K, Goldberg SR, Lluis C, Franco R, Ciruela F. Synergistic interaction between adenosine A2A and glutamate mGlu5 receptors: Implications for striatal neuronal function. Proc Natl Acad Sci USA 2002;99:11940–11945.
12. Svenningsson P, Fourreau L, Bloch B, Fredholm BB, Gonon F, Le Moine C. Opposite tonic modulation of dopamine and adenosine on c-fos gene expression in striatopallidal neurons. Neuroscience 1999;89:827–837.
13. Aoyama S, Kase H, Borrelli E. Rescue of locomotor impairment in dopamine D2 receptor-deficient mice by an adenosine A2A receptor antagonist. J Neurosci 2000;20:5848–5852.
14. Chen JF, Moratalla R, Impagnatiello F, Grandy DK, Cuellar B, Rubinstein M, Beilstein MA, Hackett E, Fink JS, Low MJ, Ongini E, Schwarzschild MA. The role of the D2 dopamine receptor (D2R) in A(2A) adenosine receptor (A(2A)R)-mediated behavioral and cellular responses as revealed by A(2A) and D-2 receptor knockout mice. Proc Natl Acad Sci USA 2001;98:1970–1975.
15. Hino T, Arakawa T, Iwanari H, Yurugi-Kobayashi T, Ikeda-Suno C, Nakada-Nakura Y, Kusano-Arai O, Weyand S, Shimamura T, Nomura N, Cameron AD, Kobayashi T, Hamakubo T, Iwata S, Murata T. G-protein-coupled receptor inactivation by an allosteric inverse-agonist antibody. Nature 2012;482(7384):237–U130.
16. Dore AS, Robertson N, Errey JC, Ng I, Hollenstein K, Tehan B, Hurrell E, Bennett K, Congreve M, Magnani F, Tate CG, Weir M, Marshall FH. Structure of the Adenosine A(2A) Receptor in Complex with ZM241385 and the Xanthines XAC and Caffeine. Structure 2011;19(9):1283–1293.
17. Jaakola VP, Griffith MT, Hanson MA, Cherezov V, Chien EYT, Lane JR, Ijzerman AP, Stevens RC. The 2.6 angstrom crystal structure of a human A(2A) adenosine receptor bound to an antagonist. Science 2008;322:1211–1217.
18. Lebon G, Warne T, Edwards PC, Bennett K, Langmead CJ, Leslie AGW, Tate CG. Agonist-bound adenosine A(2A) receptor structures reveal common features of GPCR activation. Nature 2011;474 (7352):521-U154.
19. Xu F, Wu HX, Katritch V, Han GW, Jacobson KA, Gao ZG, Cherezov V, Stevens RC. Structure of an Agonist-Bound Human A(2A) Adenosine Receptor. Science 2011;332(6027):322–327.
20. Lyman E, Higgs C, Kim B, Lupyan D, Shelleys JC, Farid R, Voth GA. A role for a specific cholesterol interaction in stabilizing the apo configuration of the human A(2A) adenosine receptor. Structure 2009;17:1660–1668.
21. Lee JY, Lyman E. Agonist Dynamics and Conformational Selection during Microsecond Simulations of the A(2A) Adenosine Receptor. Biophysical Journal 2012;102(9):2114–2120.
22. Bara-Jimenez W, Sherzai A, Dimitrova T, Favit A, Bibbiani F, Gillespie M, Morris MJ, Mouradian MM, Chase TN. Adenosine A(2A) receptor antagonist treatment of Parkinson's disease. Neurology 2003;61:293–296.
23. KHKC Ltd. Kyowa Hakko receives not approvable letter from FDA for istradefylline (KW-6002). Press Release, February 28, 2008.
24. Scheerer P, Park JH, Hildebrand PW, Kim YJ, Krauss N, Choe HW, Hofmann KP, Ernst OP. Crystal structure of opsin in its G-protein-interacting conformation. Nature 2008;455:497–502.
25. Farrens DL, Altenbach C, Yang K, Hubbell WL, Khorana HG. Requirement of rigid-body motion of transmembrane helices for light activation of rhodopsin. Science 1996;274:768–770.
26. Sheikh SP, Zvyaga TA, Lichtarge O, Sakmar TP, Bourne HR. Rhodopsin activation blocked by metal-ion-binding sites linking transmembrane helices C and F. Nature 1996;383:347–350.
27. Singh R, Hurst DP, Barnett-Norris J, Lynch DL, Reggio PH, Guarnieri F. Activation of the cannabinoid CB1 receptor may involve a W6.48/F3.36 rotamer toggle switch. J Pept Res 2002;60:357–370.
28. Shi L, Liapakis G, Xu R, Guarnieri F, Ballesteros JA, Javitch JA. Beta2 adrenergic receptor activation. Modulation of the proline kink in transmembrane 6 by a rotamer toggle switch. J Biol Chem 2002;277:40989–40996.
29. Palczewski K, Kumasaka T, Hori T, Behnke CA, Motoshima H, Fox BA, Le Trong I, Teller DC, Okada T, Stenkamp RE, Yamamoto M, Miyano M. Crystal structure of rhodopsin: A G protein-coupled receptor. Science 2000;289:739–745.
30. Warne T, Serrano-Vega MJ, Baker JG, Moukhametzianov R, Edwards PC, Henderson R, Leslie AG, Tate CG, Schertler GF. Structure of a beta1-adrenergic G-protein-coupled receptor. Nature 2008;454:486–491.
31. Burstein ES, Spalding TA, Brann MR. The second intracellular loop of the m5 muscarinic receptor is the switch which enables G-protein coupling. J Biol Chem 1998;273:24322–24327.
32. Wess J, Bonner TI, Dorje F, Brann MR. Delineation of muscarinic receptor domains conferring selectivity of coupling to guanine nucleotide-binding proteins and 2nd messengers. Mol Pharmacol 1990;38:517–523.
33. Wong SKF, Ross EM. Chimeric muscarinic cholinergic—beta-adrenergic receptors that are functionally promiscuous among G-Proteins. J Biol Chem 1994;269:18968–18976.
34. Shan JF, Weinstein H, Mehler EL. Probing the structural determinants for the function of intracellular loop 2 in structurally cognate G-protein-coupled receptors. Biochemistry 2010;49:10691–10701.
35. Arnold K, Bordoli L, Kopp J, Schwede T. The SWISS-MODEL workspace: a web-based environment for protein structure homology modelling. Bioinformatics 2006;22:195–201.
36. Eisenberg D, Luthy R, Bowie JU. VERIFY3D: Assessment of protein models with three-dimensional profiles. Macromol Crystallogr B 1997;277:396–404.

37. Case TAD, Cheatham TE, III, Simmerling CL, Wang J, Duke RE, Luo R, Crowley M, Walker RC, Zhang W, Merz KM, Wang B, Hayik S, Roitberg A, Seabra G, Kolossváry I, Wong KF, Paesani F, Vanicek J, Wu X, Brozell SR, Steinbrecher T, Gohlke H, Yang L, Tan C, Mongan J, Hornak V, Cui G, Mathews DH, Seetin MG, Sagui C, Babin V, Kollman PA. AMBER 10. San Francisco: University of California; 2008.
38. Gordon JC, Myers JB, Folta T, Shoja V, Heath LS, Onufriev A. H++: a server for estimating pK(a)s and adding missing hydrogens to macromolecules. Nucleic Acids Res 2005;33:W368–W371.
39. Humphrey W, Dalke A, Schulten K. VMD: Visual molecular dynamics. J Mol Graph 1996;14:33–38.
40. Trott O, Olson AJ. Software news and update AutoDock vina: improving the speed and accuracy of docking with a new scoring function, efficient optimization, and multithreading. J Comput Chem 2010;31:455–461.
41. Phillips JC, Braun R, Wang W, Gumbart J, Tajkhorshid E, Villa E, Chipot C, Skeel RD, Kale L, Schulten K. Scalable molecular dynamics with NAMD. J Comput Chem 2005;26:1781–1802.
42. Dupradeau FY, Cezard C, Lelong R, Stanislawiak E, Pecher J, Delepine JC, Cieplak P. REDDB: a database for RESP and ESP atomic charges, and force field libraries. Nucleic Acids Res 2008;36:D360–D367.
43. Frisch GWT, Schlegel HB, Scuseria GE, Robb MA, Cheeseman JR, Montgomery JA, Jr, Vreven T, Kudin KN, Burant JC, Millam JM, Iyengar SS, Tomasi J, Barone V, Mennucci B, Cossi M, Scalmani G, Rega N, Petersson GA, Nakatsuji H, Hada M, Ehara M, Toyota K, Fukuda R, Hasegawa J, Ishida M, Nakajima T, Honda Y, Kitao O, Nakai H, Klene M, Li X, Knox JE, Hratchian HP, Cross JB, Bakken V, Adamo C, Jaramillo J, Gomperts R, Stratmann RE, Yazyev O, Austin AJ, Cammi R, Pomelli C, Ochterski JW, Ayala PY, Morokuma K, Voth GA, Salvador P, Dannenberg JJ, Zakrzewski VG, Dapprich S, Daniels AD, Strain MC, Farkas O, Malick DK, Rabuck AD, Raghavachari K, Foresman JB, Ortiz JV, Cui Q, Baboul AG, Clifford S, Cioslowski J, Stefanov BB, Liu G, Liashenko A, Piskorz P, Komaromi I, Martin RL, Fox DJ, Keith T, Al-Laham MA, Peng CY, Nanayakkara A, Challacombe M, Gill PMW, Johnson B, Chen W, Wong MW, Gonzalez C, Pople JA. Gaussian 03. Wallingford CT: Gaussian, Inc.; 2004.
44. Wang T, Duan Y. Chromophore channeling in the G-protein coupled receptor rhodopsin. J Am Chem Soc 2007;129:6970–6971.
45. Martyna GJ, Tobias DJ, Klein ML. Constant-Pressure Molecular-Dynamics Algorithms. J Chem Phys 1994;101(5):4177–4189.
46. Ryckaert JP, Ciccotti G, Berendsen HJC. Numerical-integration of cartesian equations of motion of a system with constraints—molecular-dynamics of *N*-alkanes. J Comput Phys 1977;23(3):327–341.
47. Darden T, York D, Pedersen L. Particle Mesh Ewald—an N.Log(N) method for Ewald sums in large systems. J Chem Phys 1993;98:10089–10092.
48. Ming-Jun Yang Xue-Qin Pang, Xin Zhang, Ke-Li Han. Molecular dynamics simulation reveals preorganization of the chloroplast FtsY towards complex formation induced by GTP binding. J Struct Biol 2010;173:57–66.
49. Kabsch W, Sander C. Dictionary of protein secondary structure—pattern-recognition of hydrogen-bonded and geometrical features. Biopolymers 1983;22:2577–2637.
50. Michael Feig JK, Charles L. Brooks, III. MMTSB Tool set, MMTSB NIH research resource. The Scripps Research Institute; 2001.
51. Ballesteros JA. Integrated methods for the construction of three dimensional models and computational probing of structure function relations in G protein-coupled receptors. Methods Neurosci 1995;25:366–428.
52. Park JH, Scheerer P, Hofmann KP, Choe HW, Ernst OP. Crystal structure of the ligand-free G-protein-coupled receptor opsin. Nature 2008;45:U183–U133.
53. Rasmussen SG, Choi HJ, Rosenbaum DM, Kobilka TS, Thian FS, Edwards PC, Burghammer M, Ratnala VR, Sanishvili R, Fischetti RF, Schertler GF, Weis WI, Kobilka BK. Crystal structure of the human beta2 adrenergic G-protein-coupled receptor. Nature 2007;450:383–387.
54. Cherezov V, Rosenbaum DM, Hanson MA, Rasmussen SG, Thian FS, Kobilka TS, Choi HJ, Kuhn P, Weis WI, Kobilka BK, Stevens RC. High-resolution crystal structure of an engineered human beta2-adrenergic G protein-coupled receptor. Science 2007;318:1258–1265.
55. Dror RO, Arlow DH, Borhani DW, Jensen MO, Piana S, Shaw DE. Identification of two distinct inactive conformations of the beta(2)-adrenergic receptor reconciles structural and biochemical observations. Proc Natl Acad Sci USA 2009;106:4689–4694.
56. Higashijima T, Uzu S, Nakajima T, Ross EM. Mastoparan, a peptide toxin from wasp venom, mimics receptors by activating Gtp-binding regulatory proteins (G-proteins). J Biol Chem 1988;263:6491–6494.
57. Lechleiter J, Hellmiss R, Duerson K, Ennulat D, David N, Clapham D, Peralta E. Distinct sequence elements control the specificity of G-protein activation by muscarinic acetylcholine-receptor subtypes. EMBO J 1990;9:4381–4390.
58. Okada T, Fujiyoshi Y, Silow M, Navarro J, Landau EM, Shichida Y. Functional role of internal water molecules in rhodopsin revealed by X-ray crystallography. Proc Natl Acad Sci USA 2002;99:5982–5987.
59. Okada T, Sugihara M, Bondar AN, Elstner M, Entel P, Buss V. The retinal conformation and its environment in rhodopsin in light of a new 2.2 angstrom crystal structure. J Mol Biol 2004;342:571–583.
60. Lebon G, Warne T, Edwards PC, Bennett K, Langmead CJ, Leslie AG, Tate CG. Agonist-bound adenosine A2A receptor structures reveal common features of GPCR activation. Nature 2011;474:521–525.